Vera C. Rubin Observatory
Systems Engineering

Rubin Observatory Baseline Calibration Plan

Parker Fagrelius, and Eli S. Rykoff

SITCOMTN-086

https://doi.org/10.71929/rubin/2583850
Latest Revision: 2025-06-12

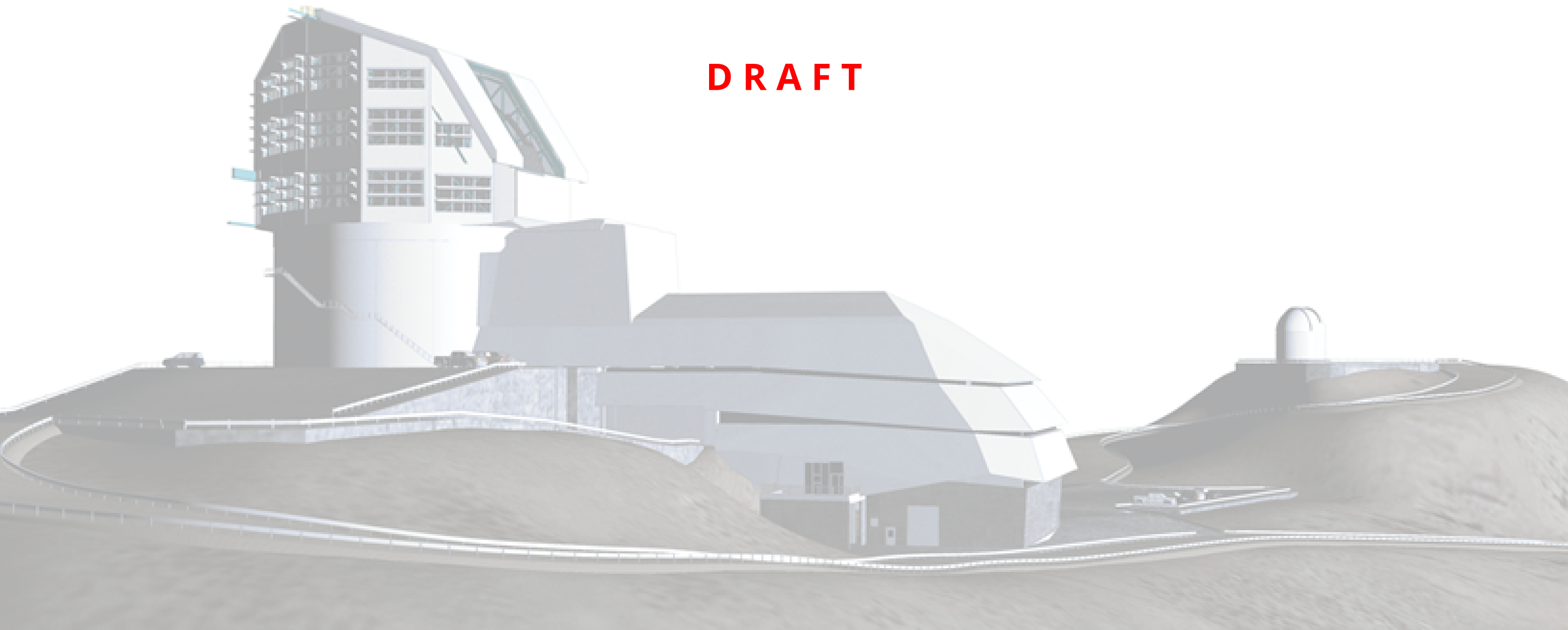

Abstract

Baseline calibration plan describing the as-built system to be delivered at the time of the Operations Readiness Review (ORR), and for use during Year 1 of the Rubin Observatory Legacy Survey of Space and Time (LSST).

Change Record

Version	Date	Description	Owner name
1	2023-XX-XX	Unreleased.	Parker Fagrelius

Document source location: `https://github.com/lsst-sitcom/sitcomtn-086`

Contents

Rubin Observatory Baseline Calibration Plan

1 Introduction

The basic question of photometric calibration of an astronomical survey is how to take raw counts output from the camera (in arbitrary Analog-Digital Units (ADU)) and convert these to calibrated fluxes in nanoJansky (nJy). In order for this procedure to yield uniform results across the camera and the sky, it must take into account variations that are both achromatic ("gray") and chromatic, that latter of which depend on the spectral energy distribution (SED) of each object. This includes variations in the atmosphere as a function of time and airmass; spatial variations in the filter and detectors; pixel size variations; and various sensor effects such as charge transfer ineffeciency (CTI) and the Brighter Fatter Effect (BFE).

This technote describes the baseline photometric calibration plan to be delivered by Rubin Construction and to be used in Data Release Production (DRP) during at least the first year of the LSST. It includes plans for performing instrumental signature removal (ISR), which is also known as "detrending"; correct flat-fielding; background/foreground subtraction; and derivation of a uniform photometric calibration over the full survey. It also includes plans for generating "calibration frames" such as biases, darks, and various types of flats, incorporating LEDs, a class 4 tunable laser, and a novel Collimated Beam Projector (CBP). We expect that this is not the final calibration plan for the LSST survey, but rather an initial baseline suitable for the first year of survey observations that will meet our required goals for photometric repeatability and uniformity. Further improvements are planned in the future to address effects such as parallel CTI, persistence, and other effects that are not mitigated by the minimal system described in this document. We plan to take as much calibration data early on in the survey with the intent to reprocess these data later with improved algorithms.

The calibration plan in this technote is heavily influenced by the Dark Energy Survey, which achieved better than 2 mmag uniformity over $5000\,\mathrm{deg}^2$ in the Southern sky (Rykoff et al., 2023). In particular, we refer the reader to Bernstein et al. (2017, henceforth B17) and Burke et al. (2018, henceforth BR18).

2 Requirements

The requirements on calibration are defined in the LSST Science Requirements Document [LPM-17]. The photometric quality and accuracy of the LSST data products is driven by four main components:

1. Relative photometry (repeatability)
2. Stability across the sky (spatial uniformity)
3. Relative accuracy (color zero-points)
4. Transfer to physical flux scale (external absolute photometry)

The requirements for photometric calibration accuracy are specified using the following error decomposition (valid in the limit of small errors):

$$m_{\text{cat}} = m_{\text{true}} + \sigma + \delta_m(x, y, \theta, \alpha, \delta, \text{SED}, t) + \Delta\, m \tag{1}$$

where m_{true} is the true magnitude defined by eqs. 4 and 7, m_{cat} is the cataloged LSST magnitude, σ is the random photometric error (including random calibration errors and count extraction errors), and $\Delta\, m$ is the overall (constant) offset of the internal survey system from a perfect AB system (the six values of $\Delta\, m$ are equal for all the cataloged objects).

Here, δ_m describes the various systematic dependencies of the internal zeropoint error around $\Delta\, m$, such as position in the field of view (x, y), the normalized system response (θ), position on the sky (α,δ), and the source spectral energy distribution(SED). Note that the average of δ_m over the cataloged area is 0 by construction.

The SRD allocates error specifications for g,r,i bands, with a 50% increase expected for u,z,y bands. These high level allocations are further broken down to three main elements in Observatory System Specifications [LSE-30]. These are Instrument Throughput, Atmospheric Transmittance, and Reference Star Catalogs. The full functional error budget can be found in LSST Document-9553.

where m$_{true}$ is the true magnitude defined by eqs. 4 and 7, m$_{cat}$ is the cataloged LSST magnitude, σ is the random photometric error (including random calibration errors and count

Design Spec (millimag)	Repeatability	Uniformity	Color Accuracy	External Absolute Photometry
Overall Specification	5	10	5	10
Instrument Throughput	3	2	3	-
Atmospheric Transmittance	3.5	4	3	-
Reference Catalog	2.5	9	3	-

Table 1: Requirements for repeatability, uniformity, color accuracy, and absolute photometric zeropoint for the LSST survey.

Design Spec (millimag)	Repeatability	Uniformity	Color Accuracy	Abs. Photometry
Overall Specification	5	10	5	10
Instrument Throughput	3	2	3	-
Atmospheric Transmittance	3.5	4	3	-
Reference Catalog	2.5	9	3	-

extraction errors), and Δm is the overall (constant) offset of the internal survey system from a perfect AB system (the six values of Δm are equal for all the cataloged objects). Here, δ_m describes the various systematic dependencies of the internal zeropoint error around Δm, such as position in the field of view (x, y), the normalized system response (θ), position on the sky (α, δ), and the source spectral energy distribution (SED). Note that the average of δ_m over the cataloged area is 0 by construction.

The SRD allocates error specifications for the griz bands, with a 50% increase expected for u and y bands. These high level allocations are further broken down to three main elements in Observatory System Specifications [LSE-30]. These are Instrument Throughput, Atmospheric Transmittance, and Reference Star Catalogs. The full functional error budget can be found in LSST Document-9553.

From these functional requirements, requirements are allocated to the Telescope & Site [LSE-60] and Data Management [LSE-61] systems to ensure that the functional requirements are met.

3 Instrumental Signature Reduction (ISR)

In this section, we describe the instrument signature removal (ISR) for LSSTCam. After the photons hit the detector surface, there are a number of sensor effects that alter the image as photoelectrons are produced, collected in the detector, clocked and read out, and sent through the amplifier(s) to the analog-to-digital converter (ADC).

In the first part of this section, we introduce a simplified model of the LSSTCam detector and readout system that we believe captures the fundamental effects. Then we describe how we apply corrections "in reverse" to go from the raw camera output of Analog to Digital Units (ADU) in 16 amplifiers to a "post ISR" image in units of electrons (e^-) that are equivalent to the number of photocarriers produced in each pixel in the camera. In this stage we do not correct for quantum efficiency as a function of wavelength, as that requires knowledge of each individual source SED. We leave the wavelength dependent effects to the photometric calibration described in Section 4.

3.1 LSSTCam Detector and Electronics Model

The LSSTCam detectors are 4k x 4k CCDs comprised of 16 amplifier segments of approximately 500 columns (the serial transfer direction) and 2000 rows (the parallel transfer direction). The amplifier segments are laid out in 2 rows of 8 amplifiers, with the "top half" amplifiers denoted "C10" through "C17" and the bottom half denoted "C00" through "C07". The amplifiers are connected via cabling to a Readout Board (REB) which has two sets of Analog Signal Processing Integrated Circuit (ASPIC) chips. [Need to confirm how many ASPICs per board and how many boards per raft, etc.] An illustration of our function model of the amplifier segments and readout electronics is in Figure 1.

The functional model is intended to be read from left to right and top to bottom. We start with an amplifier segment that has incident photons. First, as these photons are collected, we have the Brighter/Fatter Effect (BFE). This is the result of the fact that as charge accumulates in a pixel it will distort the local electric field and push later arriving photocharges away, with the net result that bright objects have a slightly broader point spread function (PSF). See Section 3.14 for more information on the correction to this effect.

Next, we note that as the exposure is integrating charge, there is some small amount of dark current that accumulates. For LSSTCam sensors this dark current is very small ($< 0.1\, e^-/s$) except for warm and hot pixels. See Section 3.13 for more information on the dark correction.

The charge is then read out by careful timing of voltages in the sequencer file. Charge is moved down into the serial register, and then out to the on-chip amplifier which has an "on chip gain" of approximately $\sim 5 \mu V/e^-$. After each row is read out the charges are transferred

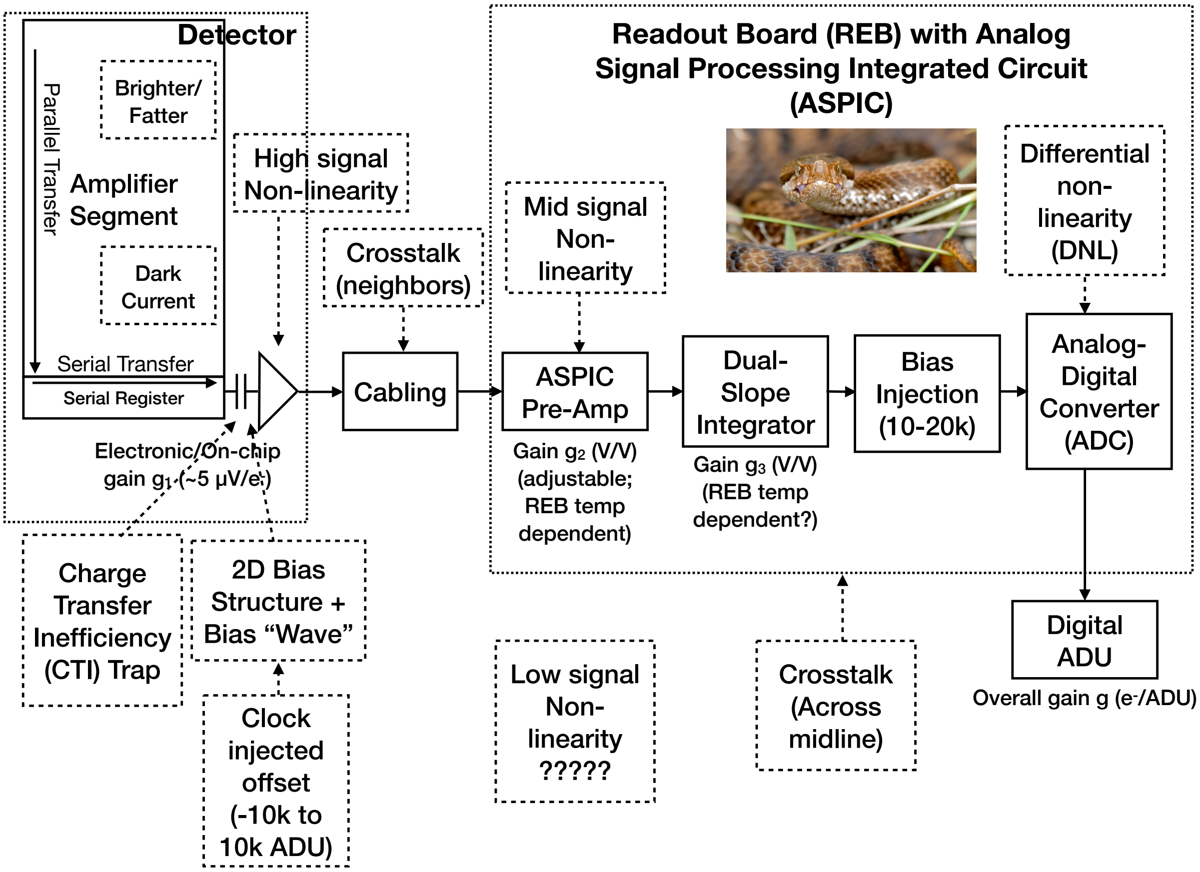

Figure 1: Model of the LSSTCam detectors and readout electronics.

in the parallel direction. The full readout of each amplifier takes around [2.2 seconds].

As charge is clocked out along the serial direction, there is a small amount of charge that is left behind. This is the “serial charge-transfer ineffeciency (sCTI)” that is corrected by a model from Snyder & Roodman (2020). Furthermore, as charge is clocked out of the amplifier segment into the on-chip amplifier there is a sharp turn in the wiring. This creates a small charge trap that can fill up and decay with a characteristic timescale. This CTI trap is also corrected by the Snyder and Roodman model. See Section 3.10 for more information on the sCTI correction.

At the same time, some amount of charge is injected into the signal chain at this location by the clock. This clock-injected offset (or serial feedthrough) has a level equivalent of -10000 to 10000 ADU, depending on the amplifier. We note that although this bias offset is injected early in the signal chain it is virtually indistinguishable from the explicit bias injection prior to digitization. Therefore, it is subtracted out with the overscan subtraction (see Sections 3.4 and 3.8). We also assume that this is the location in the signal chain where additional 2D bias structure including the bias "wave" (bias structure along the serial direction) is coming from.

The on-chip amplifier is the origin of the high-signal non-linearity (over 50000 ADU). In addition to the high-signal non-linearity, there is also some non-linearity in the mid-signal regime that comes from the ASPIC pre-amp (described below), as well as some low-signal (less than a few thousand ADU) non-linearity of unknown origin. In correction (see Section 3.9) we do not distinguish between the sources of non-linearity, and assume for the sake of simplicity that it all originates in the on-chip amplifier. Before correction the typical non-linearity is of order XX %, and after correction it is below 0.1% for the vast majority of amplifiers.

The signal next travels down a set of ribbon cables from all the amplifiers into the Readout Board and ASPIC. It is in this cabling that the crosstalk signal between neighboring amplifiers (which are in neighboring cables) appears. [get a picture of this part of the camera?] This crosstalk has some small non-linearity, as studied by Snyder (2020). There is additional crosstalk between amplifiers across the midline that is typically of the opposite sign, and comes from ASPIC-to-ASPIC interactions. We do not distinguish between these sources of crosstalk and correct them together as described in Section 3.7.

When entering the ASPIC the signal is first amplified by the ASPIC pre-amp, which has an adjustable gain (g_2) that was set so that the total gain is approximately 1.7 ADU/electron. This pre-amp has a small amount of non-linearity, and we attribute the "mid-signal" non-linearity to this amplifier. In addition, the gain of this amplifier depends slightly on the temperature of the REB, with a constant of approximately $0.06\%/C$. Under normal operating conditions the REB temperatures are kept stable so the impact of this variation is negligible.

The signal then is measured with a dual-slope integrator. [Need somebody who is not me to write a couple of sentences here]. This has another effective gain (g_3) that depends on the readout time and hence the time duration of the integration per pixel. This gain may also be temperature dependent, but that is completely degenerate with the pre-amp temperature dependence.

Next we inject some level of bias signal to ensure that all voltages are positive. The amount of bias injection varies from amp to amp, but must be at least 10000 ADU (equivalent) to ensure that we are above zero from any negative clock-injected offset.

Finally, the signal is put into an analog-to-digital converter (ADC) which provides the final digitized signal with a total effective gain g e^-/ADU. The ADC itself does not have perfect mapping from continuous voltage into digitized counts, with some “codes” preferred over others. At the moment we do not correct for this differential non-linearity (DNL) in the ADC. However, we plan to in the future.

3.2 ISR Ordering

The output of the camera for each detector contains 16 different amplifier images, each with a data region and serial and parallel overscan pixels, all of which have units of digitized ADU. The goal of instrumental signature removal is to reverse the ordering of the detector effects and obtain an image representing the photoelectron map as they originally hit the surface of the detector. In some cases we cannot exactly reverse the order of the model. For example, we treat all crosstalk as coming from one location in the signal chain (the cabling between the detector and the REB), and we treat all non-linearity as coming from the output amplifier on the detector. In addition, we cannot separate the different locations of bias structure injected into the overscan. The flowchart outlining our ISR pipeline is in Figure 2. In some cases we cannot exactly reverse the order of the model.

3.3 Dithering Digitized Counts

The raw amplifier images are in units of digitized ADU. The ADU are only an approximation of the voltage input to the ADC due to the digitization. These digitized integer values can be difficult to work with, particularly when doing overscan subtraction, due to their discrete nature. Therefore, our first step is to offset the digitization by applying a “dithering” procedure where we add a uniform random value from $[-0.5, 0.5)$ to each pixel (with a seed based on the unique exposure identification number). This dithering adds approximately $1/12$ ADU of noise, and in exchange we see reduced row-to-row and column-to-column correlations after overscan, crosstalk correction, and gain correction. In the future we would like to offset the digitization with a full DNL look-up table that can map each ADU to a range of input voltages.

3.4 Serial Overscan Correction

We now run serial overscan correction to remove the overall bias level in each amplifier, including the injected bias signal. Due to the fact that many channels in LSSTCam are not com-

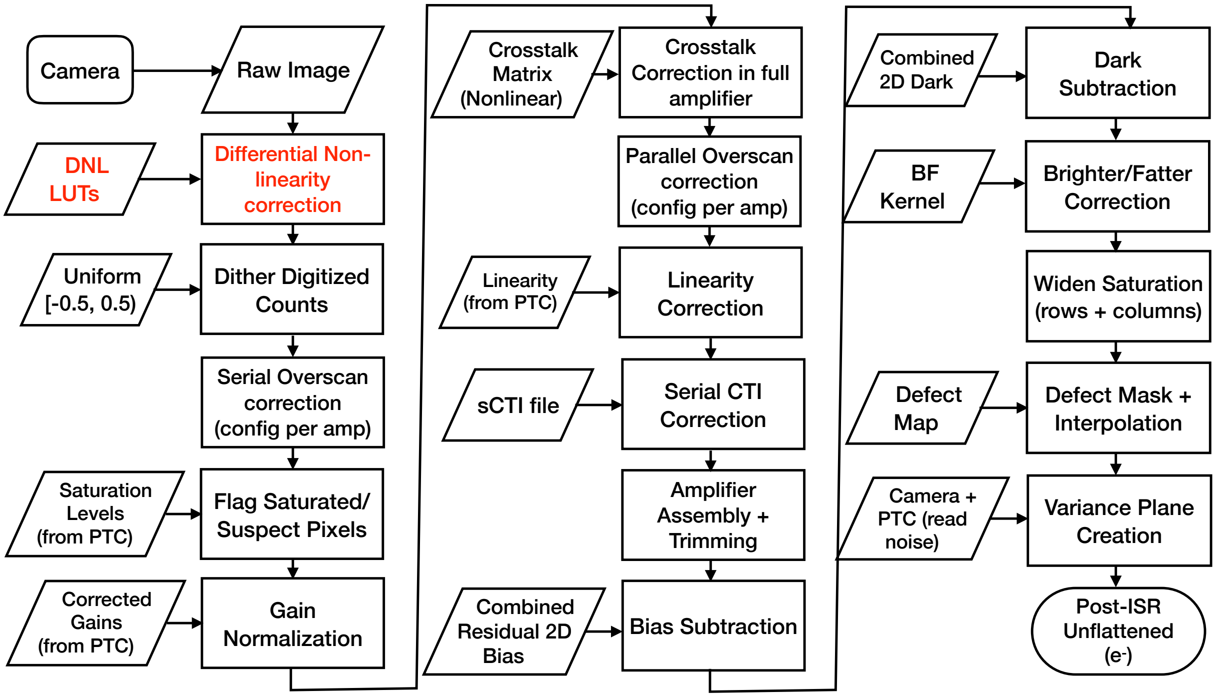

Figure 2: Instrument Signature Reduction Flow Chart.

pletely stable with time, our default processing mode is to perform row-by-row serial overscan correction to remove this bias level as well as possible bias drifts and jumps. We have 64 overscan pixels per row, and we have XX overscan pixels per column. We take the median of each row, skipping the first 3 and final 3 columns to avoid pixels with residual charge-transfer-inefficiency (CTI) which bleeds into the serial overscan region.

3.5 Saturation Flagging

After serial overscan correcton, we flag pixels that are deemed to be "saturated" to ensure that these pixels are masked and interpolated correctly in the following ISR steps. There are many possible definitions of saturation, and we have decided to use the photon transfer curve (PTC) turnoff as our initial saturation estimate. This is the level at which the variance of a pixel deviates significantly from Poisson, and appears to be a good approximation of when blooming/bleeding starts to occur for point sources.

During ComCam commissioning, we noticed some additional behavior in the ITL detectors regarding saturation that requires special handling. First of all, when a bright star has a saturated bleed trail that hits the edge of the detector it both spreads out with a characteristic trumpet-shaped "edge bleed" pattern, and also "sags" such that the level of the charge bleed is both well above the sky level but also well below the nominal saturation level. Therefore we have specialized code to identify these edge bleeds and mask them. Second of all, in cases where a not-quite-as-bright star has a bleed trail that comes close to but not at the edge the obviously saturated trail can in some cases drop down below the saturation level. In these cases we detect these columns and mark the full column as saturated for downstream processing.

3.6 Gain Normalization

Up to this point in the processing chain, all operations are performed with ADU units. In this step we convert the units of each amplifier from ADU to e^- using the gain measurement from the PTC analysis (Astier et al., 2019). This location in the processing chain is necessarily approximate because there is another gain factor (the electronic on-chip gain) that is upstream, we apply the full gain factor here because the REB applies most of the gain when converting from voltages to ADU. All downstream calibration products are either produced in e^- units, or are adjusted using the gain values to ensure consistent application of crosstalk, linearity, CTI, etc.

In the future, we may apply corrections to the gain based on REB temperature (as mentioned above), or other factors that we find that have a predictable impact on the gain. At the moment we have not found this to be necessary during ComCam processing despite the fact that the REBs were not temperature controlled as is the case with LSSTCam.

3.7 Crosstalk Correction

After correcting for the gain in the ASPIC, we correct the crosstalk signal which has its primary origin in the ribbon cabling between the REB and the detector. As discussed previously, this part of the signal chain in the model is prior to the input to the ASPIC and therefore the natural units are e^-.

The crosstalk signal is corrected with a full matrix for each detector that describes the effect of each "source" amplifier on every "target" amplifier. Amplifiers on the same side of the detector that share a REB have larger crosstalk signal than those that are on different REBs. In addition to the standard linear crosstalk signal, there is a non-linearity in the crosstalk response of the LSSTCam amplifiers. These are modeled as a first-order correction to the crosstalk matrix as a function of source signal level (Snyder, 2020).

In the future we may be able to decompose different crosstalk signals in different parts of the signal chain, and would update the sequence of ISR steps accordingly.

[Need a paragraph on subtrahend masking]

3.8 Parallel Overscan Correction

For many amplifier channels we need to additionally perform parallel overscan subtraction due to additional unstable structure in the bias. One particular challenge of the parallel overscan subtraction is that hot columns and saturated stars bleed into the parallel overscan region, making these columns unusable for overscan subtraction. In addition, these bright signals may inject a crosstalk signal into the other overscan regions. That is why we perform parallel overscan subtraction after the crosstalk correction over the full frame, including overscan regions.

We take considerable care in masking parallel overscan pixels that may be contaminated by bleed trails and significant residual crosstalk, while ensuring that structured bias signal is properly removed. One of the primary assumptions is that bleeds are always positive deviations in the parallel overscan region, while significant negative deviations are primarily from bias structure. When a column is masked we do a simple interpolation from neighboring unmasked columns.

3.9 Linearity Correction

The response of the readout system is not completely linear, with non-linearities at difference signal levels injected at different parts of the signal chain, as described in Section 3.1. For the sake of simplicity, we apply the linearity correction at the location of the largest source of non-linearity, which is at the output amplifier from the detector.

Our linearity correction model is a multi-node spline as originally defined by P. Astier (personal communication). The linearity correction per amplifier is derived from a series of flat pairs illuminated at different flux levels and contamporaneously monitored by a reference photodiode. After the full linearity correction we find residuals below the 0.05% level, some of which can be attributed to uncertainty in the photodiode measurements.

3.10 CTI Correction

Now that we have corrected the linearity, the next instrument signature to remove is the serial charge transfer inefficiency (sCTI) according to the Snyder and Roodman model, which is primarily caused by the wiring coming out of the detector. The sCTI model is calibrated with the "extended pixel edge response" (EPER) measurement that measures how much imaging charge from flat-field images leaks into the serial overscan region. We additionally use the first pixel in the serial overscan region to fix the sCTI in the imaging region.

3.11 Imaging Region Assembly

At this stage we no longer have any need for the serial and parallel overscan regions, and the processed image is trimmed to only include the on-sky imaging region for the detector. Various statistics including mean, median, and standard deviations are computed for the overscan and residual overscan regions and these are stored in the image metadata.

3.12 Bias Subtraction

After correcting for the effects described above, there may be some residual imprint of some bias structure. To generate a bias frame, which will be subsequently subtracted from the image our goal is to take a series of ~ 400 zero-second integration frames, perform the above ISR correction described above on each frame independently, and then compute the clipped mean per pixel. This is what we call a "combined bias frame". Note that it is important to perform crosstalk correction prior to bias frame creation to ensure that the crosstalk signal from hot columns is corrected or else these will get imprinted on all of the amplifier segments which is undesirable.

3.13 Dark Subtraction

We now subtract off the residual dark current, based on the effective dark time of the exposure, which may be slightly longer than the open-shutter exposure time. The dark current is computed by taking a series of ~ 400 30 second exposures with the shutter closed (to match the typical survey exposure integration time), and taking a clipped mean combination after rejecting cosmic rays in the dark images. The typical dark current is very small for the vast majority of amplifiers (XX electrons per second), necessitating such a large set of inputs to get a significant estimate of the dark current. The dark current may be larger for some amplifiers or warm regions, as well as for warm pixels.

3.14 Brighter-Fatter Correction

We now correct for the final instrument signature, the Brighter/Fatter effect. The BF correction is naturally in units of e^{-} as it is the outcome of charge accumulating in the detector pixels. To derive the BF kernel for correction we make use of the fact that the BF creates pixel-to-pixel correlations in flat-field images. Therefore, we can use the flat-field image pairs that are used to derive the PTC gain and linearity correction as an input to the BF kernel generation code. See Broughton et al. (2024) for details on our algorithm for estimating the BF kernel as well as correcting for the BF effect in pixel images.

We note that because the BF kernel is a non-local effect, we cannot apply a correction near the detector edges and must interpolate over any known bad or saturated pixels prior to applying the correction. The interpolation in this stage may be more aggressive than we want in the final image, and therefore interpolated pixels are restored to their original values (plus the correction value) after BF processing. All pixels near a detector edge that cannot be corrected by the BF kernel are marked with the `EDGE` mask bit.

3.15 Defect Masking and Interpolation

At this stage in the processing we do our final interpolation over saturated and defect pixels. These saturated and defect pixels are not used downstream, but the interpolation is done to help create better images for visual inspection that do not have the dynamic range ruined by unusable pixels.

Defects are all marked with the `BAD` mask bit. The defects themselves are derived from an initial combined bias, dark, and flat field image. We look for pixels with significant flux ($>$ 1000 ADU) in the bias; hot pixels that have a flux of at least $3\,e^{-}/s$ in the dark; and cold pixels that have at least a 5% deficit in the flat. In addition, we mask all pixels that are within 5 pixels of the detector edge as defects to avoid the very strong gradient in pixel size caused by lateral electric fields in these regions. Finally, we have scanned the focal plane for unusual defects that are best masked manually.

3.16 Variance Plane Creation

We now estimate the variance plane of the image. This is computed by starting with the gain-corrected image itself, assuming Poisson variance. We additionally add in quadrature the read noise per amplifier which was estimated from the PTC analysis above. Our variance plane therefore includes variance from the sources themselves. One consequence of having 16 amplifiers per detector with different gains and read noise values is that while the image itself should not show any amplifier boundaries after processing, the final variance plane will show amplifier boundaries due to the different noise characteristics of each amplifier segment.

3.17 Applying Flat Fields

After the above series of steps, we have an unflattened, gain normalized image with sensor effects removed. As flat fielding is intrinsically connected to photometric calibration, we defer the discussion of how flat fields are used to Sections 4.4.1 and 4.8.

4 Photometry with Chromatic Corrections

The fundamental goal of photometric calibration is to estimate the surface brightness of sources across the full sky in a uniform way, as would be measured at the top of the atmosphere (TOA). Our general outline for uniform photometry follows DES and specifically B17 and BR18. Our ground-based telescope will count only a fraction of photons from a celestial source that reaches the top of the Earth's atmosphere after attenuation from the atmosphere, filters, optics, and detector quantum efficiency.

Our overall photometry plan follows BR18, in particular the use of the Forward Global Calibration Method (FGCM; Burke et al., 2018). This global calibration algorithm uses repeated observations of stars in multiple bands, through multiple instrumental and atmospheric bandpasses, to simultaneously constrain the atmospheric model as well as standardized TOA star fluxes over a wide range of star colors.

4.1 Chromatic Corrections

For broadband observations through the u, g, r, i, z, y filters, the number of photoelectrons (e^-) produced by a source in a pixel is proportional to the integral of the TOA flux $F_\nu(\lambda)$ (the source spectral energy distribution, or SED) weighted by the observation transmission function, $S_b(x, y, \text{alt}, \text{az}, t, \lambda)$ in a given filter b. We discuss the effect of integrating over the point spread function (PSF) and pixel size variations below.

$$e_b^- = A \int_0^{\Delta T} dt \int_0^{\infty} F_\nu(\lambda) S_b(x, y, \text{alt}, \text{az}, t, \lambda) \frac{d\lambda}{h_{\text{Pl}}\lambda}, \tag{2}$$

where A is the area of the telescope pupil and ΔT is the duration of the exposure. The position x, y is the location in the focal plane; alt, az are the altitude and azimuth of the observation (the altitude being the more important driver of the variation of the transmission by the atmosphere as a function of airmass). The units of flux $F_\nu(\lambda)$ are erg cm^{-2} s^{-1} Hz^{-1}, and the factor $\frac{d\lambda}{h_{\text{Pl}}\lambda}$ counts the number of photons per unit energy at a given wavelength, where h_{Pl} is Planck's constant.

Following BR18, we definte the "observed passband", which is position- and time-dependent, as such:

$$S_b^{\text{obs}} \equiv S_b(x, y, \text{alt}, \text{az}, t, \lambda). \tag{3}$$

Following Fukugita et al. (1996) we define the AB magnitude of a source to be:

$$m_b^{\text{obs}} = -2.5 \log_{10} \left(\frac{\int_0^\infty F_\nu(\lambda)\, S_b^{\text{obs}}\, \lambda^{-1} d\lambda}{\int_0^\infty F^{\text{AB}}\, S_b^{\text{obs}}\, \lambda^{-1} d\lambda} \right), \tag{4}$$

where $F^{\text{AB}} = 3631$ Jy. Putting this together with the above equation and simplifying we get:

$$m_b^{\text{obs}} = -2.5 \log_{10}(e_b^-) + 2.5 \log_{10}(\Delta T) + 2.5 \log_{10}(\mathscr{I}_0^{\text{obs}}) + \text{ZPT}^{\text{AB}}, \tag{5}$$

where

$$\mathrm{ZPT}^{\mathrm{AB}} = 2.5\log_{10}\left(\frac{A\,F^{\mathrm{AB}}}{h_{\mathrm{Pl}}}\right), \tag{6}$$

and $Iobs$ is defined as the integral over the observed passband b:

$$\mathcal{I}_0^{\mathrm{obs}}(b) \equiv \int_0^\infty S_b^{\mathrm{obs}}(\lambda)\,\lambda^{-1}\,d\lambda. \tag{7}$$

Note that in the formulation so far we are limited by the variety of observed passbands that are encountered in a survey, due to variations in instrument over the focal plane and atmosphere over time. Furthermore, these equations require knowledge of the wavelength dependence of the source SED. Therefore, we define a "standard" magnitude as the broadband magnitude that would be measured if a given source were observed through a standard passband $Sstd$ that we are free to choose:

$$m_b^{\mathrm{std}} \equiv -2.5\log_{10}\left(\frac{\int_0^\infty F_\nu(\lambda)\,S_b^{\mathrm{std}}\,\lambda^{-1}\,d\lambda}{\int_0^\infty F^{\mathrm{AB}}\,S_b^{\mathrm{std}}\,\lambda^{-1}\,d\lambda}\right). \tag{8}$$

The difference between this standard magnitude and the observed magnitude is then:

$$\delta_b^{\mathrm{std}} \equiv m_b^{\mathrm{std}} - m_b^{\mathrm{obs}} = 2.5\log_{10}(\mathcal{I}_0^{\mathrm{std}}(b)/\mathcal{I}_0^{\mathrm{obs}}(b)) + 2.5\log_{10}\left(\frac{\int_0^\infty F_\nu(\lambda)\,S_b^{\mathrm{obs}}(\lambda)\,\lambda^{-1}\,d\lambda}{\int_0^\infty F_\nu(\lambda)\,S_b^{\mathrm{std}}(\lambda)\,\lambda^{-1}\,d\lambda}\right), \tag{9}$$

where $\mathcal{I}_0^{\mathrm{std}}$ is defined as in Eqn. 7.

The decomposition in Eqn. 9 is very useful. First of all, the first term is independent of the SED, and the SED-dependent "chromatic correction" is entirely in the second term. Second, the chromatic correction term goes to zero if either (a) the source SED is completely flat (as with the reference AB spectrum or (b) the observed passband $S_b^{\mathrm{obs}}(b)$ is equal to the standard passband $S_b^{\mathrm{std}}(b)$. Therefore, it is important to choose a standard passband as close to the "typical" observing conditions as possible in order to minimize the chromatic corrections, and to ensure that averaging over many observed passbands tends toward the mean (standard) passband. For LSSTCam this is made more challenging by the different shapes of the QE curves of the two types of detectors (E2V and ITL), and so we must decide whether to choose one or the other shape as the standard, or to "split the baby" and choose something in the middle that is representative of neither. We will explore the options during commissioning, as the optimal decision depends on the as-built performance of the spatial varying throughput due to vignetting and filter variations.

4.2 Observed Passbands

We assume that the instrumental and atmospheric components of the observed passband are independent, and therefore we can decompose S_b^{obs} as such:

$$S_b^{\mathrm{obs}}(\lambda) = S_b^{\mathrm{inst}}(x, y, t, \lambda)\, S^{\mathrm{atm}}(\mathrm{alt}, \mathrm{az}, t, \lambda), \tag{10}$$

where S_b^{inst} is the instrumental component that depends on location in the detector and focal plane, as well as time and wavelength, and S_b^{atm} is the atmospheric component that depends on pointing in the sky. We address each of the instrumental and atmospheric transmission curves in turn.

4.3 Instrumental Response

We can decompose the instrumental response into different parts that depend on the focal plane and time in different ways. Our initial decomposition is:

$$S_b^{\mathrm{inst}}(x, y, t, \lambda) = k_b\, S^{\mathrm{refflat}}(x, y, \lambda)\, S^{\mathrm{optics}}(t, \lambda)\, S^{\mathrm{CBP}}(x, y, \lambda), \tag{11}$$

where S^{refflat} is the “reference flux flat” that normalizes the system response to focused light; S^{optics} describes the change in the opacity of the optical system over time; S^{CBP} is the in-situ chromatic throughput of the system as measured by the collimated beam projector; and k_b is an overall throughput constant at the start of the survey that can be determined with observations of standard stars/white dwarfs.

4.3.1 Change in Opacity of Optical System

We break out the $S^{\mathrm{optics}}(t, \lambda)$ as a separate component, because to first order the dust on the optics and mirror build up smoothly over time, more frequently than we can or want to determine “absolute” calibrated throughput measurements. In the original DES formalism described in BR18 this was only a gray term without wavelength dependence, with offsets determined whenever there was a mirror wash or hardware change. Further experience with DES and Hyper Suprime Cam Special Survey Program (HSC; need ref) demonstrated that the mirror coating degrades chromatically over time due to molecular changes. This chromatic change is visible in all bands, but is most dramatic in the bluest bands. Therefore, we must allow a smooth degradation of S^{optics} as a function of wavelength (estimated as a first-order correction; I have to put the math somewhere in here).

4.3.2 In-situ Measurements of Chromatic Throughput from CBP

The term S^{CBP} describes the in-situ chromatic estimate (with an arbitrary normalization) from the “static” CBP: including the filter (as a function of wavelength and position); the mirrors M1, M2, and M3 (as a function of wavelength); the lenses L1, L2, ?? (as a function of wavelength); and the detector quantum efficience (QE) as a function of position. For Y1 calibrations we assume that $S^{\mathrm{CBP}}(x, y, \lambda)$ is constant for each detector, and will refine this in future versions of the calibration system. Overall, we expect that the CBP measurements should agree with lab data for detector QE and vendor measurements of filter throughput as a function of position. Note that we could use monochromatic flats like the DECal system (ref) to achieve the same in-situ chromatic throughput estimation, although ghosting due to unfocused light makes this much easier with the CBP.

4.4 Background Flats

We denote the background flat as $S^{\mathrm{bkg}}(x, y)$, which is the image required to flatten the focal plane image for background subtraction. The background flat can be effectively approximated from the “dome flat” which is obtained by meauring the response to a Lambertian source of light such as the dome screen.

Each detector has different chromatic response overall, and within each detector. Therefore, without any further SED adjustments, the quality of the flattening from the background flat depends on how well matched the flat-field SED is to the sky SED. In the future, this will be handled by synthesizing SED-matched background flats from monochromatic flats. At the present time we are exploring a first-order correction based on illuminating the flat-field screen with multiple LEDs of different spectra that overlap different parts of each filter bandpass.

4.4.1 Reference Flux Flats

The term S^{refflux} is the reference flux flat which normalizes the response to focused light (see, e.g. B17). Nominally, this has chromatic variations at small scales, particularly in the bluer bands, but for Y1 we are assuming any chromatic variations are assumed to be constant at the detector scale and described by the $S^{\mathrm{CBP}}(\lambda)$. Therefore, this term is just the achromatic (gray) portion of the instrumental throughput which can vary from pixel to pixel.

The reference flux flat has a few key differences from the dome flat or background flat. First of all, the dome flat contains a factor of the pixel area $\Omega(x, y)$, which means that it assumes pixel size variations are QE variations. Second, there are differences in focused and scattered light patterns from a flat field screen and distant sky sources. Finally, the SED of the dome flat does not match the reference spectrum. This final problem we will fix in future data processing by synthesizing broadband flats from monochromatic flats illuminated by the in-dome laser. We are also exploring a first-order correction based on multiple LEDs, as with the background flat. In spite of all these challenges, we will start our creation of the reference flux flat with the dome flat as dome flats are the most efficient way of measuring the relative response of all the billions of pixels in LSSTCam on small scales.

The dome flat is a good start for estimating the reference flux flat, but has issues at both small scales and large scales. At small scales, there are lateral electric field effects such as “tree rings” and the “picture frame” that are pixel size variations that show up as apparent QE variations in the dome flat. At large scales, the response to focused light is different than the dome flat which includes unfocused and scattered light.

To handle lateral electric field effects we fit templates based on our physical knowledge of the detectors. This includes radial templates for tree rings with a fixed center, and square templates around the edge of the detectors. The exact methodology is TBD, and may not be in place by the end of commissioning.

To handle the larger scale illumination correction for LSST Y1 we use a “star flat” generated from a sequence of multi-band dithered observations of a moderately dense star field. These observations are cross-calibrated using FGCM to generate per-detector polynomial approximations of the throughput relative to the dome flat at scales of tens of pixels and greater. By making use of stars of various colors, the FGCM solution can approximate the star flat terms for a flat reference spectrum.

The illumination correction is then generated per-band from the star flat and the pixel area variations determined from the Jacobian of the world coordinate system (WCS) from the camera model. This becomes:

$$S^{\text{illum}}(x, y) = \frac{1.0}{S^{\text{star}}(x, y)\,\Omega(x, y)}, \tag{12}$$

where $S^{\text{illum}}(x, y)$ is the illumination correction, $S^{\text{star}}(x, y)$ is the star flat, and $\Omega(x, y)$ is the pixel area field. The reference flux flat then becomes:

$$S^{\text{refflux}}(x, y) = S^{\text{dome}}(x, y)\,S^{\text{illum}}(x, y), \tag{13}$$

where $S^{\text{dome}}(x, y)$ is the dome flat.

We find it convenient for visualization to apply the dome flat / background flat at the end of the ISR stage, such that we get:

$$e^{-\text{bkg}}_{b}(x, y) = \frac{e^{-}_{b}(x, y)}{S^{\text{dome}}(x, y)}, \tag{14}$$

where $e^{-}_{b}(x, y)$ is the unflattened count of electrons per pixel (in band b), and $e^{-\text{bkg}}_{b}(x, y)$ is the background-flattened image.

Similarly, the photometrically-flattened image $e^{-\text{phot}}_{b}(x, y)$ is:

$$e^{-\text{phot}}_{b}(x, y) = \frac{e^{-}_{b}(x, y)}{S^{\text{refflux}}(x, y)}. \tag{15}$$

Putting this together we have:

$$e^{-\text{phot}}_{b}(x, y) = \frac{e^{-}_{b}(x, y)}{S^{\text{dome}}(x, y)\,S^{\text{illum}}(x, y)}. \tag{16}$$

In practice, we make use of the background-to-photometric ratio, which is equal to the illumination correction:

$$\frac{e^{-\text{bkg}}_{b}(x, y)}{e^{-\text{phot}}_{b}(x, y)} = S^{\text{illum}}(x, y). \tag{17}$$

This means that we need to apply (or unapply) the illumination correction in our pipelines whenever we want to do flux measurements vs background subtraction. In the end our images with the illumination correction (reference flux flat) applied are in “fluence” (electron counts per pixel) units and not “surface brightness” units (electron counts per pixel per steradian), as this procedure divides by the pixel area $\Omega(x, y)$.

For LSST Y1 we use a constant illumination correction for a given band for all images within a given range of time (as long as possible). In the future we plan to synthesize a new background-to-photometric ratio for every image given the background SED (based on solar elevation and lunar illumination). The software to perform this analysis will not be ready by the completion of construction and will be developed in the early years of the LSST.

4.5 Atmosphere Response

The attenuation of light due as it propagates through the atmosphere includes absorption and Rayleigh scattering from molecular constituents (primarily O_2 and O_3); absorption by preciptable water vapor (PWV), Mie scattering by airborne particulate aerosols that have physical sizes comparable to the wavelength of visible light; and shadowing by ice crystals and water droplets in clouds that is independent of wavelength.

This can be summarized with the following equation:

$$S^{\text{atm}}(\text{alt}, \text{az}, t, \lambda) = S^{\text{molecular}}(\text{bp}, \text{zd}, t, \lambda)\, S^{\text{PWV}}(\text{zd}, t, \lambda)\, e^{-(X(\text{zd})\, \tau(t,\lambda))}, \tag{18}$$

where $S^{\text{molecular}}$ is the absorption and scattering from dry gasses (primarily in the u, g, and r bands); S^{PWV} is the absorption by water vapor (primarily in the z and y bands); τ is the aerosol optical depth (AOD); X is the airmass; and bp is the barometric pressure.

Following FGCM, we obtain the molecular scattering using MODTRAN (Berk et al., 1999) combined with the barometric pressure, which is obtained as part of the standard suite of weather data at Cerro Pachon. Ozone absorption can be parameterized by one parameter per night. All constituent throughputs are computed as a function of zenith distance (airmass) in finite steps and interpolated at each wavelength step.

The PWV may vary through the night and as a function of position in the sky. In the FGCM default model the PWV is allowed to vary via a smooth quadratic function through the night. It may also be estimated per visit in the z and y bands by using the relative shift of stars of different colors. As above, we use MODTRAN to determine the absorption as a function of wavelength for a grid of PWV and zenith distance values which are then interpolated.

The aerosol model is a simple Angstrom model with one particular species:

$$\tau(\lambda) = \tau_{7750}\,(\lambda/7750\,\text{Å})^{-\alpha}, \tag{19}$$

where the normalization τ_{7750} and optical index α depend on the density, size, and shape of the particulates. As with PWV, the AOD normalization is allowed to vary linearly through the night, while the optical index is given a single night.

4.6 Auxiliary Telescope

The Auxiliary Telescope (AuxTel) will be in operation during the LSST survey, obtaining contemporaneous estimates of the atmospheric throughput via low resolution spectroscopy of bright (sixth magnitude) stars. The mode of operation of AuxTel has not yet been finally determined. We are likely to use different modes in observing when LSST is targeting $ugri$ bands (where more care needs to be taken with the aerosols and ozone) and when LSST is targeting the zy bands (where we need to know the PWV to high precision).

In the first iteration, we plan on using the AuxTel model outputs to validate the FGCM atmospheric model which is determined from the broadband multi-color photometry of the stars observed on a given night. In the future, we may use AuxTel to provide priors on the atmospheric model fit. Considerable care will have to be taken to ensure that outliers from the spectroscopic fits do not contaminate the model used in the broadband photometry. We do not plan to use satellite measurements of atmospheric constituents as priors as the resolution is low enough to be contaminated by observations of neighboring valleys rather than the mountain peak where the telescope is sited.

4.7 Integrating Over Sources

This short section will discuss PSF modeling and aperture photometry and the finite size of stars (and galaxies) and the care that needs to be taken with fluence or surface density images, following B17.

4.8 Foregrounds and Backgrounds

What to do about foregrounds and backgrounds, including fringes? These needs to be written.

4.9 Global Calibration

5 Flat Field System

6 CBP

Flatfield system consists of four main parts: a calibration screen, an aspheric reflector optic, a tunable laser and a white light system.

The calibration screen will be illuminated by either the white light system or a tunable laser. The white light system will be used for daily flats, while the tunable laser will be used to create monochromatic flats. Both illumination systems are mounted on the dome and co-rotate with the calibration screen. The output of each is co-located at the center of the calibration screen and can be switched between. In order to project that light onto the screen, an additional optic is mounted on the back of the camera and pancake wrap. This is located precisely 3 meters from the projector. It is critical that the projector is aligned with the reflector to ensure a flat illumination pattern on the calibration screen.

6.1 Calibration Screen

The calibration screen is a large reflective surface that can be aligned with the primary mirror and send diffuse light directly to the telescope and camera. It is large enough to illuminate the whole telescope at one time. The surface itself has a diameter of 10.27 meters and an inner diameter of 3.18 meters. Of this area, the section from a diameter of 4.18 - 9.27 meters is coated with a highly reflective material. The outer and inner rings are coated with a very absorptive material. The screen is built of several small panels, with 16 panels making the outer ring and 8 panels making the inner ring. They are secured to a structure such that they are all flat to 3mm across the whole surface. The panels are coated with Labsphere Permaflect 94% and 5% respectively.

The structure on which the panels are mounted can rotate from 0 to -23 degrees relative to horizontal using an actuator. In this way, it can be tilted so that the optical axis of the telescope aligns with the optical axis of the screen. There will also be 4 retroreflectors mounted around the screen that can be seen by a laser tracker that is mounted on the telescope so that the screen can be easily aligned with the telescope on a daily basis.

Requirements for the screen can be found in LTS-523 and drawings can be found in LTS-126.

6.2 Reflector

The optic that is used to illuminate the calibration screen in full takes the shape of an asphere, which is a radially symmetric optic with a radius of curvature that varies radially. The Rubin Observatory aspheric reflector optic was made from a single piece of aluminum, which was necessary given it's unique shape. The shape of the asphere is given by the following function:

$$Z(s) = \frac{Cs^2}{1 + \sqrt{1 - (1 + k)\,C^2 s^2}} + A_4 s^4 + A_6 s^6 + \ldots \tag{20}$$

where Z is the sage of the surface parallel to the optical axis, s is the radial distance from the optical axis, C is the curvature, k is the conic constant, and A_n are the aspheric coefficients. For this asphere, $C = 1/551.4041743$, $k = -3.92683047$, $A_4 = 0$, and $A_6 = -3.737203 \times 10^{-18}$.

The shape and reflectivity of the optic were measured in the laboratory. The shape was found to match the function within a micron. The reflectivity and scatter from the optic does change across the optic, varying in reflectance from 78 - 82% across the optic.

As mentioned above, the reflector is mounted on the back side of the camera and the pancake wrap. It is mounted on its own hexapod, which can be adjusted manually. When installed, it will be carefully aligned with the optical axis of the telescope, using this hexapod, and then secured in place.

The reflector has a cover which can be opened by command using linear actuators.

6.3 Tunable Laser

The tunable laser is an Ekspla NT242 and capable of producing light from 300 - 2600 nm in 1 nm steps (see fig. 3). It does this by using a combination of a tunable parametric stage using OPO crystals and a sum frequency generation stage. Addiitonally, this laser has a spectral cleaning unit, which slightly reduces the output power but increases the spectral purity by removing some of the primary and secondary harmonics using a prism. The laser interfaces to a Fiber Coupling unit, which makes is easy to switch between outputs, two of which focus the light into fibers. In this way, we can easily switch between sending the light to the flat field or the Collimated Beam Projector.

The laser is designed to operate in room temperature air (18-25°C). It will be housed in an aluminum structure mounted to the dome near the calibration screen and sitting below the CBP. The laser will be kept within this operating temperature range as much as possible using heaters used in a small area (<100W). After use of the laser, heat will be removed from the enclosure using fans until the enclosure is within 2 degrees of the ambient dome environment. The laser light will be fed into a NA 0.22 optical fiber (Ceramoptic WFNS) and travel ∼ 15 m from the laser platform to the CBP and central projector.

The laser can be operated in continuous mode or burst mode. The pulse duration is 3-6 ns, with a repetition rate of 1000 Hz. In continuous mode it will continue to send pulses at this rate. In burst mode, you can select a number of pulses sent in a “burst”, after which it will not emit until you tell the laser to send another burst.

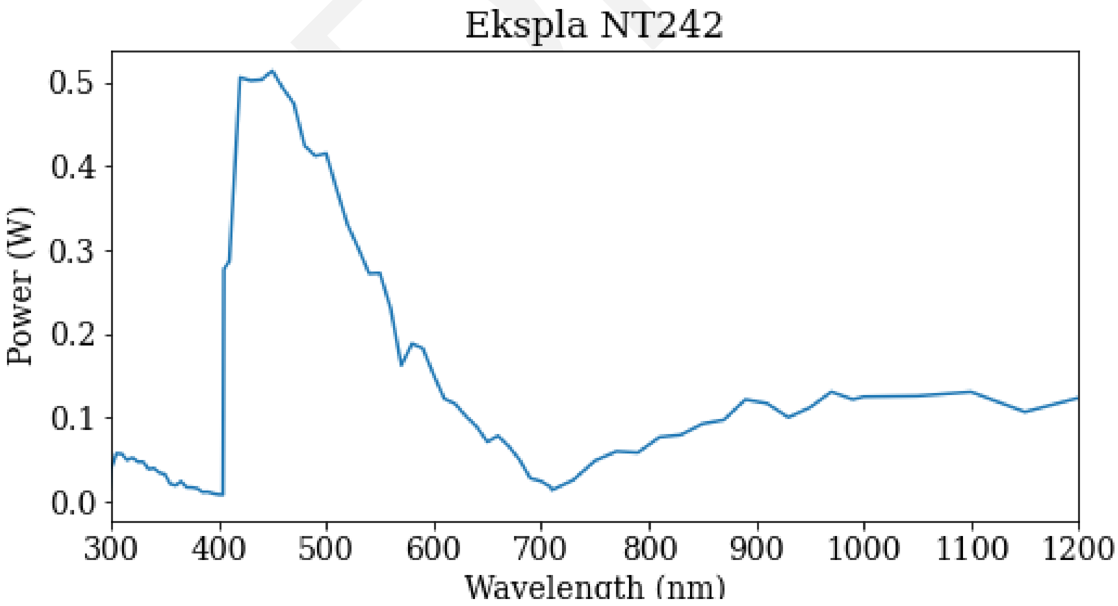

Figure 3: Expected Power output of NT242 Tunable Laser

6.4 White Light System

plot of LEDs Mechanical configuration Optical model Model output

6.5 Projector

6.6 Monitoring systems

We will want to measure precisely how much light from the laser is entering the CBP at a given wavelength so that we determine the exact fraction of that light that is captured by the LSST camera. In order to do that, we need to monitor the luminosity of the laser as it enters the integrating sphere as well as the spectral properties of the light. This data will be recorded for every measurement made with the CBP in such a way that it can be easily linked to the LSST camera image.

6.6.0.1 Photodiode In order to monitor the exact amount of light injected into the CBP, we use a Hamamatsu S2281 Silicon Photodiode that has been precisely calibrated by NIST. This photodiode, which is mounted directly to the integrating sphere, has a sensitive area of 11 mm in diameter. It is read out by a Keithley 6517b electrometer. The electrometer can measure current, charge, resistance and voltage. Our uses of the CBP will likely use the charge and current modes.

The electrometer can be read out as quickly as every 20 ms. There is a relationship between how long of an exposure you can take and the integration time. At the minimum integration time, you can take an exposure of ~30 seconds. The data is saved in a fits file in the lfa with the elapsed time from the start of the exposure and the value measured. The range can be set to any value from X to Y.

6.6.0.2 Fiber Spectrograph The spectral response of the injected light will be measured by a pair of fiber-fed spectrographs from Avantes SensLine, one for the blue wavelengths (range) and one for the red (range). These spectrographs will actually be housed in the central projection area in the center of the calibration screen. This is where light from the laser can be projected on the calibration screen. The fibers will be situated such that they will measure some fraction of reflected light within the projector box. When we want to measure the spectral response of the light, we will inject the fiber that runs to the calibration screen, take our measurement, and then send the laser light to the CBP. This assumes that the spectral response will not change from one output to another, which we will have to confirm.

The data from the spectrographs will be saved in a fits file in the lfa that will include the wavelength array and the counts measured by the spectrograph at that spacing.

7 CBP

The Rubin CBP was built by DFM Engineering [1]. The design is essentially a Schmidt camera used in reverse. It includes a primary mirror of 33cm diameter, Schmidt Corrector and a 3-element Flat Field Corrector. It produces a beam with an aperture of 24.1 cm and a field of view of 4.1 degrees. The focal length of the CBP is 625mm, and with the LSST focal length at 10.1m, the magnification factor is 16. Therefore, a 100μm pinhole on the CBP would correspond to 1600 μm, or 160 pixels.

Aperture	24.1 cm
Focal Length	62.5 cm
Field of View	4.1 degrees

Table 2: CBP Specifications

The mount of the CBP allows movement in Azimuth and Elevation, with a swing diameter of 1.32 meters. The locations are controlled by a Galil Digital Motor Controller (DMC) that is mounted on the azimuth housing. It controls the motors, reads the encoders, and interfaces to the control computer over ethernet. Additionally, the DMC controls the focus of the primary mirror and changes and rotates the masks. The azimuth and elevation stages are absolutely encoded with a Renishaw 26-bit on axis encoder.

At the focal plane sits the mask stage, which can hold 5 different masks. The masks can be rotated, driven by worm gears such that all masks are rotated on a common shaft by a single motor. The center mask stage is position encoded using a Renishaw absolute rotary encoder. The mask holder can hold masks with a diameter of 50 mm. Each mask will be laser etched into aluminium and are removable/interchangeable.

---

[1] https://www.dfmengineering.com

Major Subsystem Drawing:

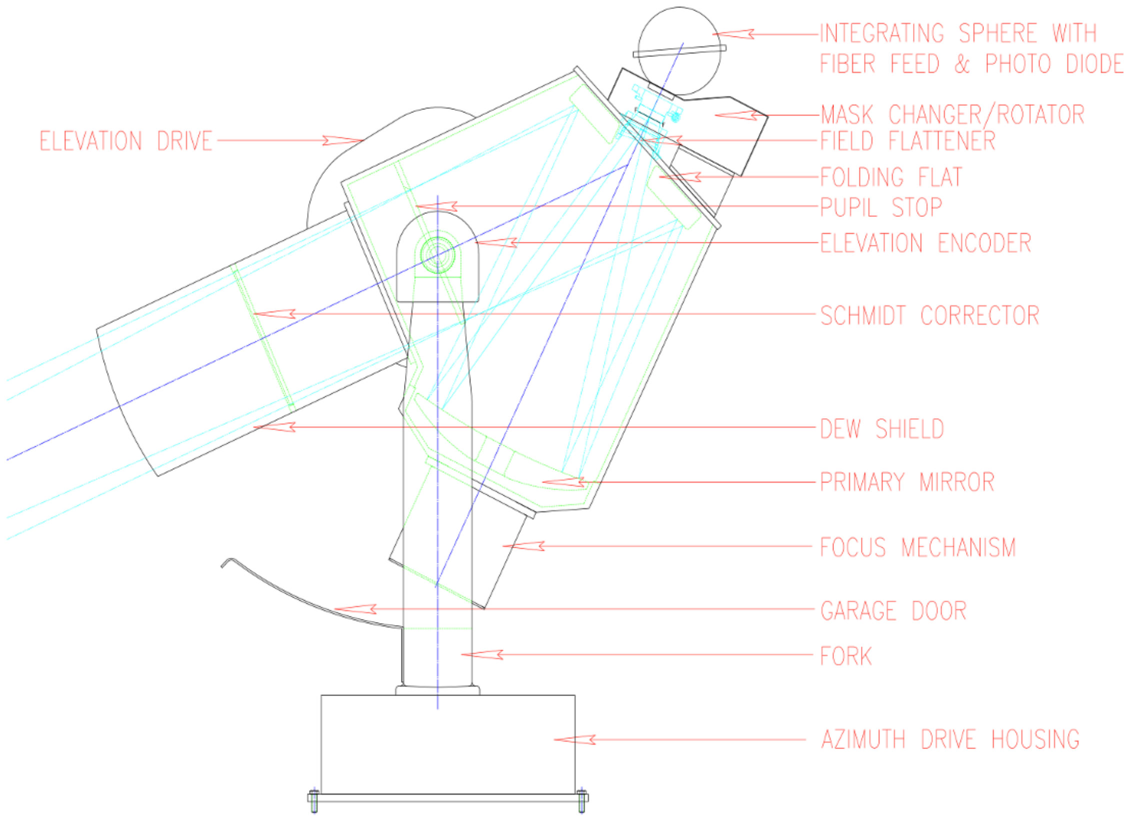

Figure 4: CBP Major subsystems

The current Integrating Sphere installed on the CBP is a Labsphere 3P-GPS-060-SF. This integrating sphere has an interior diameter of 6 in. (152.4mm) and an exit port of 2.5 in. (63.5 mm), coated with spectraflect coating. In the exit port a photodiode will be mounted and it will be illuminated by an optical fiber. The integrating sphere is held to the mask stage with standoffs. It sits ~ 7.5 cm from the focal plane/mask. Using `https://www.labsphere.com/wp-content/uploads/2021/09/Integrating-Sphere-Theory-and-Applications.pdf` as a guide to calculate the intensity of light exiting the integrating sphere by multiplying Ls by the flux incident on the integrating sphere.

8 Plans Post-Year 1

Evolution of the calibration system beyond LSST year 1.

8.1 Synthetic SED matched flats

8.2 Full CBP dataset

A Calibration Products List

Quantity	Product Description
Bias	(combined)
Dark	(combined)
CTI	what are these?
PTC	Linearity + Gain
$\mathbf{C}_i$	Crosstalk Matrix
	Defect masks
BF	Brighter-fatter kernels
	Fringe templates (zy)
	Lateral e-field templates
$\mathbf{QE}_{det}$	Sensor QE
$\mathbf{R}_{mirror}$	Mirror reflectivity (Silver x3)
$\mathbf{T}_{filter}$	Filter transmission
	"White" light flats (ugrizy)
$\mathbf{T}(\text{det}, \lambda)$	Transmission
	Dust flat (?)
	Twilight flats (ugrizy; combined)
	Sky flat (combined; ugrizy)
	Reference Flux Flat
	Dense dithered star field + lateral e-field (ugrizy)
	Survey observations

B References

Astier, P., Antilogus, P., Juramy, C., et al., 2019, A&A, 629, A36 (`arXiv:1905.08677`), doi:10.1051/0004-6361/201935508, ADS Link

Berk, A., Anderson, G.P., Bernstein, L.S., et al., 1999, In: Larar, A.M. (ed.) Optical Spectroscopic Techniques and Instrumentation for Atmospheric and Space Research III, vol. 3756 of Society of Photo-Optical Instrumentation Engineers (SPIE) Conference Series, 348–353, doi:10.1117/12.366388, ADS Link

Bernstein, G.M., Abbott, T.M.C., Desai, S., et al., 2017, PASP, 129, 114502 (`arXiv:1706.09928`), doi:10.1088/1538-3873/aa858e, ADS Link

Broughton, A., Utsumi, Y., Plazas Malagón, A.A., et al., 2024, PASP, 136, 045003 (`arXiv:2312.03115`), doi:10.1088/1538-3873/ad3aa2, ADS Link

Burke, D.L., Rykoff, E.S., Allam, S., et al., 2018, AJ, 155, 41 (`arXiv:1706.01542`), doi:10.3847/1538-3881/aa9f22, ADS Link

[LSE-30], Claver, C.F., The LSST Systems Engineering Integrated Project Team, 2018, *Observatory System Specifications (OSS)*, Systems Engineering Controlled Document LSE-30, NSF-DOE Vera C. Rubin Observatory, URL `https://ls.st/LSE-30`

[LSE-61], Dubois-Felsmann, G., Jenness, T., 2019, *Data Management System (DMS) Requirements*, Systems Engineering Controlled Document LSE-61, NSF-DOE Vera C. Rubin Observatory, URL `https://lse-61.lsst.io/`

Fukugita, M., Ichikawa, T., Gunn, J.E., et al., 1996, AJ, 111, 1748, doi:10.1086/117915, ADS Link

[LTS-523], Ingraham, P., 2019, *Calibration Screen Design and Fabrication Specifications*, Telescope & Site Controlled Document LTS-523, NSF-DOE Vera C. Rubin Observatory, URL `https://ls.st/LTS-523`

[LPM-17], Ivezić, Ž., The LSST Science Collaboration, 2018, *LSST Science Requirements Document*, Project Controlled Document LPM-17, NSF-DOE Vera C. Rubin Observatory, URL `https://ls.st/LPM-17`

[Document-9553], LSST Systems Engineering Team, 2011, *LSST Photometric Calibration Functional Error Budgets*, Informal Construction Document Document-9553, NSF-DOE Vera C. Rubin Observatory, URL `https://ls.st/Document-9553`

[LTS-126], LSST Telescope and Site Team, 2014, *Calibration Screen Assembly to Dome Interface Drawing*, Telescope & Site Controlled Document LTS-126, NSF-DOE Vera C. Rubin Observatory, URL `https://ls.st/LTS-126`

Rykoff, E.S., Tucker, D.L., Burke, D.L., et al., 2023, arXiv e-prints, arXiv:2305.01695 (`arXiv:2305.01695`), doi:10.48550/arXiv.2305.01695, ADS Link

[LSE-60], Sebag, J., Krabbendam, V., 2018, *LSST Telescope and Site (TS) Requirements*, Systems Engineering Controlled Document LSE-60, NSF-DOE Vera C. Rubin Observatory, URL `https://ls.st/LSE-60`

Snyder, A., Roodman, A., 2020, arXiv e-prints, arXiv:2001.03223 (`arXiv:2001.03223`), doi:10.48550/arXiv.2001.03223, ADS Link

Snyder, A.K.L., 2020, *Characterization of LSST camera sensor effects during integration and testing*, Ph.D. thesis, Stanford University, California, URL `https://purl.stanford.edu/jy639yg0904`

C Acronyms

Acronym	**Description**
2D	Two-dimensional
ADC	atmospheric dispersion corrector
ADU	Analogue-to-Digital Unit
ASPIC	Analog Signal Processing Integrated Circuit
CBP	Collimated Beam Projector
CTI	Charge Transfer Inefficiency
DES	Dark Energy Survey
DRP	Data Release Processing
E2V	Teledyne
FGCM	Forward Global Calibration Method
GPS	Global Positioning System
HSC	Hyper Suprime-Cam
ISR	Instrument Signal Removal
ITL	Imaging Technology Laboratory (UA)
L1	Lens 1
L2	Lens 2
LPM	LSST Project Management (Document Handle)
LSE	LSST Systems Engineering (Document Handle)
LSST	Legacy Survey of Space and Time (formerly Large Synoptic Survey Telescope)
LSSTCam	LSST Science Camera
LTS	LSST Telescope and Site (Document Handle)
M1	primary mirror
M2	Secondary Mirror
M3	tertiary mirror

MODTRAN	MODerate resolution TRANsmission model
NIST	National Institute of Standards and Technology (USA)
ORR	Operations Readiness Review
PSF	Point Spread Function
PTC	Photon Transfer Curve
QE	quantum efficiency
REB	Readout Electronics Board
SED	Spectral Energy Distribution
SF	Structure Function
SRD	LSST Science Requirements; LPM-17
TBD	To Be Defined (Determined)
WCS	World Coordinate System